Mon. Not. R. Astron. Soc. **000**, 1–14 (2015) Printed 28 September 2015 (MN LATEX style file v2.2)

# Dust within the nuclear star cluster in the Milky Way

S. Chatzopoulos[1⋆], O. Gerhard[1], T. K. Fritz[2], C. Wegg[1], S. Gillessen[1], O. Pfuhl[1], F. Eisenhauer[1]

[1] *Max Planck Institut fur Extraterrestrische Physic, Postfach 1312, D-85741, Garching, Germany*
[2] *Department of Astronomy, University of Virginia, 530 McCormick Road, Charlottesville VA 22904-4325, USA*



Submitted 2015 April 14

**ABSTRACT**

The mean absolute extinction towards the central parsec of the Milky Way is $A_K \simeq 3$ mag, including both foreground and Galactic center dust. Here we present a measurement of dust extinction *within* the Galactic old nuclear star cluster (NSC), based on combining differential extinctions of NSC stars with their $v_l$ proper motions along Galactic longitude. Extinction within the NSC preferentially affects stars at its far side, and because the NSC rotates, this causes higher extinctions for NSC stars with negative $v_l$, as well as an asymmetry in the $v_l$-histograms. We model these effects using an axisymmetric dynamical model of the NSC in combination with simple models for the dust distribution. Comparing the predicted asymmetry to data for $\sim 7'100$ stars in several NSC fields, we find that dust associated with the Galactic center mini-spiral with extinction $A_K \simeq 0.15-0.8$ mag explains most of the data. The largest extinction $A_K \simeq 0.8$ mag is found in the region of the Western arm of the mini-spiral. Comparing with total $A_K$ determined from stellar colors, we determine the extinction in front of the NSC. Finally, we estimate that for a typical extinction of $A_K \simeq 0.4$ the statistical parallax of the NSC changes by $\sim 0.4\%$.

**Key words:** galaxy center, nuclear cluster, kinematics and dynamics, dust, extinction.

## 1 INTRODUCTION

Nuclear star clusters (NSC) are located at the centers of most spiral galaxies (Carollo et al. 1998; Böker et al. 2002). Their study became possible via high spatial resolution observations from HST in the 1990s. They have properties similar to those of globular clusters although they are more compact, more massive and on average 4 mag brighter than the old globular clusters of the Milky Way (Böker et al. 2004; Walcher et al. 2005). Many NSCs host an AGN (Seth et al. 2008) i.e. a supermassive black hole (SMBH) in their centers, have complex star formation histories (Rossa et al. 2006; Seth et al. 2006) and obey scaling-relations with host galaxy properties as do central SMBHs (Ferrarese et al. 2006; Wehner & Harris 2006).

The study of NSCs is of great interest because several of the most extreme physical phenomena occur within them such as SMBHs, active galactic nuclei, star-bursts and extreme stellar densities. The Galactic NSC is particularly interesting because of its proximity. At a distance of about 8kpc from Earth it is the only NSC in which individual stars can be resolved.

The center of the galactic NSC harbors a SMBH (Genzel et al. 2010; Ghez et al. 2008). Joint statistical analysis based on orbits around Sgr A* (Gillessen et al. 2009), star counts and kinematic data gives $M_\bullet = (4.23\pm0.14)\times10^6 M_\odot$ and a statistical parallax $R_0 = 8.33\pm0.11$ kpc (Chatzopoulos et al. 2015). Recent studies (Schödel et al. 2014; Chatzopoulos et al. 2015) have revealed that the NSC is flattened with an axial ratio $q \approx 0.73$, which is consistent with the kinematic data (Chatzopoulos et al. 2015).

Observations of the NSC at optical-UV wavelengths are not feasible because of the high extinction $A_V \geqslant 30$ mag due to interstellar dust (Scoville et al. 2003; Fritz et al. 2011). Therefore we rely on the infrared, with average K-band extinction toward the central parsec close to $A_K \approx 3$ (Rieke et al. 1988; Schödel et al. 2010; Fritz et al. 2011). This is mostly foreground extinction; however, it is very difficult observationally to measure the extinction variation along the line-of-sight within the NSC.

The area around Sgr A* contains ionized gas which can be well described by a system of ionized streamers or filaments orbiting Sgr A* (Ekers et al. 1983; Serabyn & Lacy

⋆ E-mail: sotiris@mpe.mpg.de, gerhard@mpe.mpg.de

1985) that is also associated with hot dust (Lau et al. 2013). This complex structure of ionized gas is called the 'mini-spiral' and consists of four main components: the northern arm, the eastern arm, the western arm and the bar (Zhao et al. 2009), surrounded by the circumnuclear disk of inner radius $\sim 1.6$pc (Jackson et al. 1993; Christopher et al. 2005).

In our previous dynamical study of the NSC, an asymmetry in the $v_l$-proper motions was observed in the histograms which was attributed to dust causing stars on the far side of the NSC to fall out of the sample. The aim of this paper is to present estimates for the extinction within the NSC based on our dynamical model and see to what extent this is correlated with the mini-spiral, to try to understand the slight asymmetry in the $v_l$ velocity histograms of the NSC, and to check the impact of this on the fundamental parameters derived from the dynamical model such as the mass and the distance.

In section 2 we discuss briefly our recent dynamical model of the NSC and describe qualitatively the effects of dust on the observed dynamics of the NSC. In section 3 we show evidence based on the dynamics for the presence of dust within the NSC. In section 4 we develop a method for making an analytical model for the dust extinction that can be used on top of an existing dynamical model. Finally in section 5 we present extinction values for the dust within the NSC based on the prediction of the model in conjunction with the mini-spiral observations.

## 2 EFFECTS OF DUST ON THE APPARENT DYNAMICS OF THE NSC

In this section we give a brief description of the recent dynamical model of the NSC from Chatzopoulos et al. (2015) (Section 2.1) and we show initial evidence for dust extinction within the NSC (Section 2.2).

### 2.1 Axisymmetric dynamical model of the NSC

The dynamical model of the NSC described in Chatzopoulos et al. (2015) is an axisymmetric model including flattening and rotation which is an excellent match to histograms of proper motions and line-of-sight velocities in many bins on the sky. For the density model we used a two-component spheroidal $\gamma$-model (Dehnen 1993; Tremaine et al. 1994) which we fitted to the star count surface density data in ($l$, $b$) provided by Fritz et al. (2014). The inner rounder component can be considered as the NSC and the outer, more flattened component as the inner part of the nuclear stellar disk. Using the density we applied axisymmetric Jeans modeling in order to constrain the stellar mass $M_*$, the black hole mass $M_\bullet$, and the distance $R_0$ of the NSC which we found to be

$$\begin{aligned} &M_*(r<100'') = (8.94 \pm 0.31|_{\rm stat} \pm 0.9|_{\rm syst}) \times 10^6 M_\odot \\ &M_\bullet = (3.86 \pm 0.14|_{\rm stat} \pm 0.4|_{\rm syst}) \times 10^6 M_\odot \\ &R_0 = 8.27 \pm 0.09|_{\rm stat} \pm 0.1|_{\rm syst} {\rm kpc} \end{aligned} \quad (1)$$

for the NSC only, not including the constraints from stellar orbits around Srg A*.

Having this information we used the Qian et al. (1995) algorithm to calculate the even part of the 2-Integral distribution function (DF) $f(E, L_z)$. This allowed us to calculate the velocity profiles (VP) of the model. We found that the even part of the DF can predict very well the characteristic 2-peak shape (Schödel et al. 2009; Fritz et al. 2014) of the velocity histograms (VH) for the $v_l$ proper motion velocities, as well as the VHs in $v_b$. The addition of a suitable odd part in $L_z$ to the even part of the DF represents the rotation of the cluster, so that also the $v_{\rm los}$ can be reproduced.

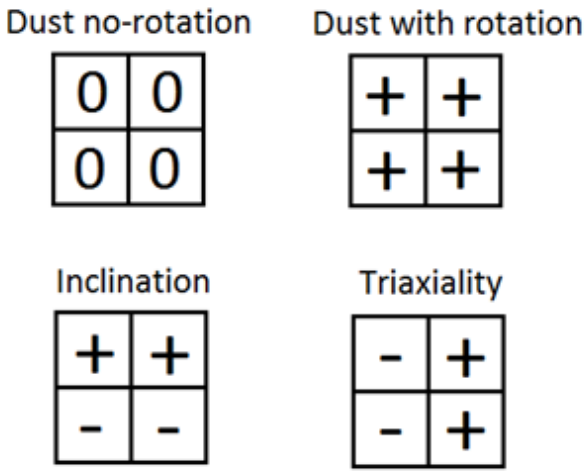


**Figure 2.** Figure illustrating the velocity profile asymmetries discussed in the text. Each small square represents a quadrant in the $(l, b)$ coordinate system, a '+' signifies an asymmetry in the $v_l$ VHs (e.g. right peak higher) a '−' the opposite asymmetry and '0' no asymmetry at all. Only dust produces the same asymmetry in every quadrant.

### 2.2 Asymmetry of the $v_l$ proper motion histograms

Upon a closer look at the velocity histograms in $l$ direction (VH$_l$) (see Fig.1) it is noticeable that the right peak is often slightly higher than the left peak. Seemingly there are more stars in the front of the cluster (positive velocities) than in the back.

The proper motion data are from Fritz et al. (2014). They are given in Galactic longitude $l^*$ and Galactic latitude $b^*$ angles centered on Sgr A*. In the following we always refer to the shifted coordinates but will omit the asterisks for simplicity. We assume that the rotation axis of the NSC is aligned with the rotation axis of the Milky Way disk. This is in accordance with the very symmetric Spitzer surface density distribution of Schödel et al. (2014).

At least three effects could produce an asymmetry as in Fig. 1. Figure 2 illustrates the effect of dust extinction without rotation, dust extinction with rotation, inclination and triaxiality on the VHs. Each small square represents a quadrant of the shifted Galactic coordinate system $(l, b)$ where Sgr A* is at the center. A '+' signifies an asymmetry (e.g. right peak higher), a '−' the opposite asymmetry, and '0' no asymmetry at all (both peaks same height). We will see in the following Sections that dust with rotation produces the same asymmetry in every quadrant. Because of the dust

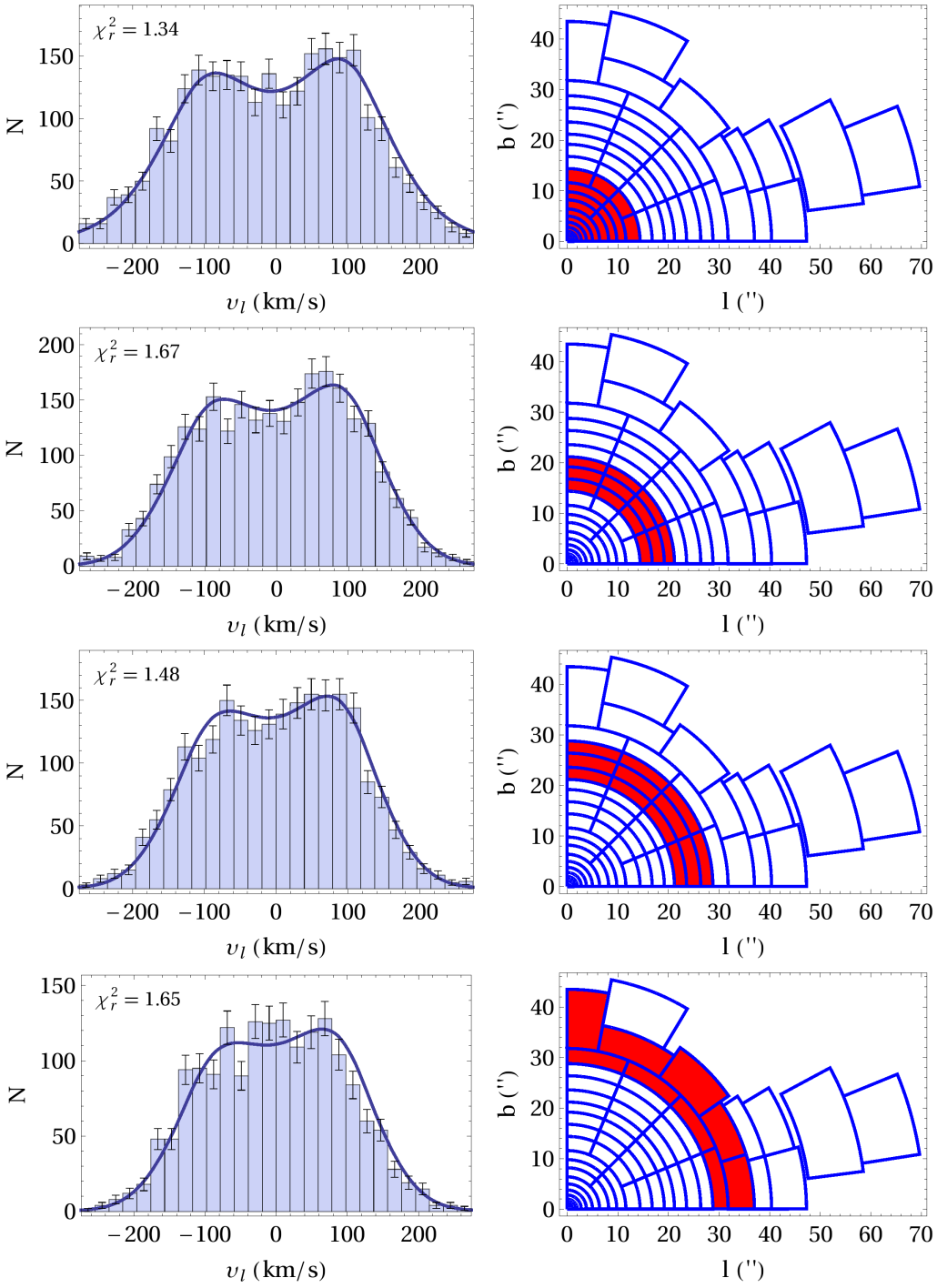


**Figure 1.** Histograms of $v_l$ proper motions and VPs predicted by an axisymmetric dynamical model of the NSC combined with a dust extinction model. The data and cells are as in Chatzopoulos et al. (2015). Each star is mapped to the first quadrant using $(l, b) \rightarrow (|l|, |b|)$. The smooth blue lines are derived from the recent model of Chatzopoulos et al. (2015) averaged over the cells combined as shown in the right panels, to which is added a homogeneous dust model with total $A_K = 0.4$, extending from $-100''$ to $+100''$ along the line-of-sight(see Section 5).

fewer stars will be visible at the back of the cluster, and because of the rotation the missing stars will be stars with negative velocities. Inclination of the NSC produces opposite results for the upper and lower quadrants, because when the line-of-sight does not pass exactly through the center, it passes through areas of unequal density in front of and behind the NSC. Finally, triaxiality produces opposite results for the right and left quadrants: consider a triaxial system with long axis in the Galactic plane but rotated away from the line-of-sight to the observer, with a triaxially symmetric rotation field. If the stars at the front of the cluster lead to

a higher peak for $v_l > 0$ on the $l > 0$ side, say, then by symmetry the opposite will be true on the $l < 0$ side.

Therefore, if we symmetrize the data to one quadrant only, the effect of the dust will remain while the effects of the inclination and triaxiality will cancel out, as illustrated in Fig. 2. This is what we observe for the symmetrized data of the NSC (Fig. 1). Therefore we conclude that the observed asymmetry cannot be a result of inclination and triaxiality but that it may be produced by dust extinction in conjunction with rotation. We note here that in order to observe this asymmetry (right peak higher than left) in the velocity profile in the $l$ direction ($VP_l$), the dust should be *inside* the cluster (i.e. within a few parsecs of the Galactic center) where the density is maximum, otherwise only a change in scale of the VPs would take place.

## 3 DIFFERENTIAL EXTINCTION IN THE NSC

For the work reported in the following, we use photometric data in the $H$ and $K$ bands and proper motions for 7101 stars from Fritz et al. (2014). We split the data into a central and an extended field. The central field is a square centered on Sgr A* with size of $40''$ and contains 5847 stars. The rest of the stars belong to the extended fields, as shown in Fig. 3.

### 3.1 Total extinction

We obtain the extinction towards each star from the $H-K$ color (stars without H photometry and early-type stars are excluded). We obtain intrinsic color estimates by assuming that the stars are at the distance of the Galactic Center and that they are giants, as it is the case for most stars in the Galactic Center (Pfuhl et al. 2014). The intrinsic color varies between 0.065 and 0.34 but the majority of stars belong to a small magnitude range around the red clump. Therefore and also because the extinction is high, the influence of intrinsic color uncertainties on the extinction is small compared to other effects, like photometric uncertainties. We use the extinction law of Fritz et al. (2011), implying $A_{\rm K} = 1.348\, E(H-{\rm K})$.

In this work we are mainly interested in the extinction variation $A_{\rm K}$ *within* the Galactic center. We obtain an estimate for that by measuring for each star the extinction relative to its neighbors, more specifically relative to the median extinction of its 15 closest neighbors. Obvious foreground stars were already excluded in Fritz et al. (2014). By using 15 neighbors we obtain a robust median extinction estimate that is much less affected by extinction variations in the plane of the sky. To further reduce the influence of this extinction variation we exclude stars with too few close neighbors.

Fig. 3 shows a map of interpolated total extinction for the central and extended fields based on $H-K$ colors. The area within the white frame is the central field which is consistent with Fig. 6 of Schödel et al. (2010). Most of the extinction of typically $A_K = 3$ mag shown in this plot is foreground extinction but a fraction $\simeq 0.4$ mag or so is intrinsic to the NSC region as we show in the following. Fig. 4 shows a histogram of the extinction for the central field. The mean extinction inferred from this plot is $A_K = 2.94$ mag with

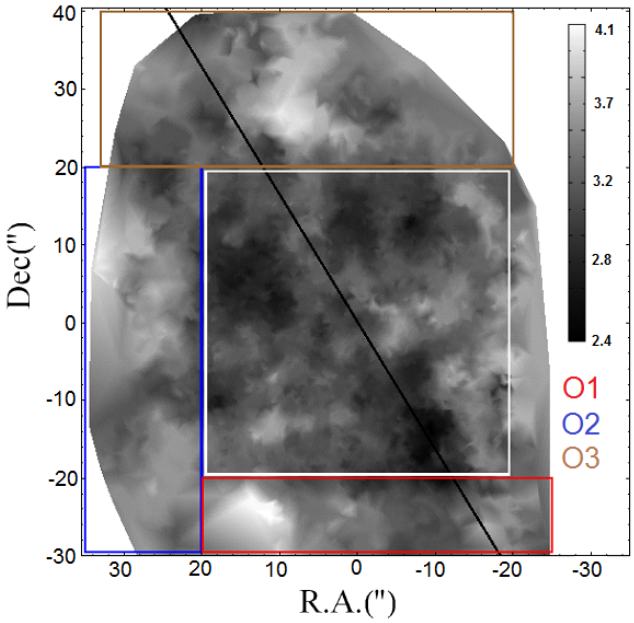


**Figure 3.** Map of $A_K$ for the NSC derived from $H-K$ colors. The map is similar to that of Schödel et al. (2010). The Galactic plane is shown as a black line. The central field is shown in white and the outer fields O1-O3 in red, blue and brown.

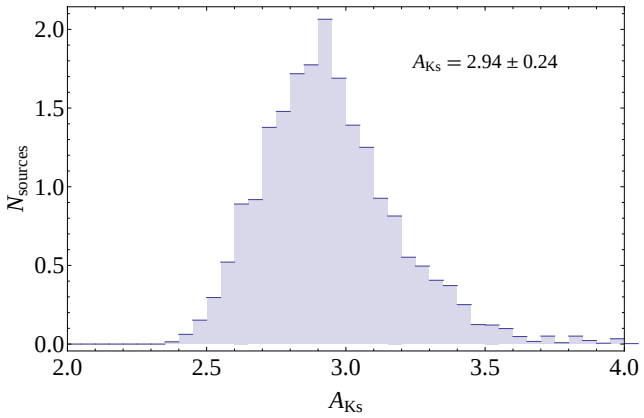


**Figure 4.** Histogram of the extinction $A_K$ based on $H-K$ colors for all the stars. Mean extinction and standard deviation also given. Stars with small $A_K$ are excluded because they are foreground stars (Fritz et al. 2014).

standard deviation 0.24 mag. This extinction value is very close to the value $A_K = 2.74$ measured by Schödel et al. (2010). The difference stems partly from the slightly different extinction laws and partly from the difference in areal coverage. Using the same law as Schödel et al. (2010) results in $A_K = 2.85$.

### 3.2 Extinction in the NSC region

The average differential extinction of stars as a function of $v_l$ and $v_b$ velocities is an important photometric quantity that can also be modeled and gives us information about

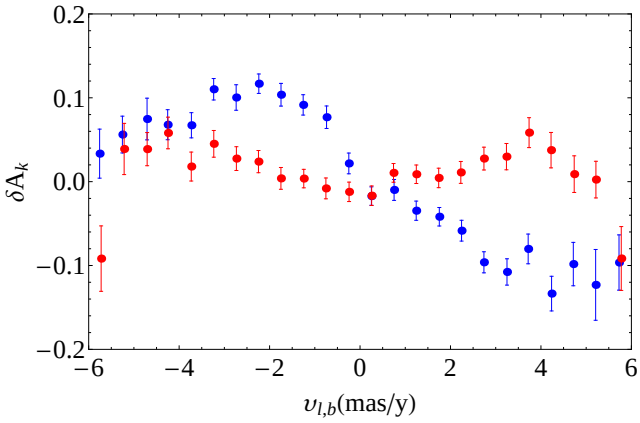


**Figure 5.** Average differential extinction of nuclear cluster stars plotted as a function of $v_l$(blue) and $v_b$(red) proper motion. The differential extinction is inferred from the difference in the color of a star to the median of its 15 nearest neighbors using the extinction law of Fritz et al. (2011) and correcting also for the weak color variation with magnitude.

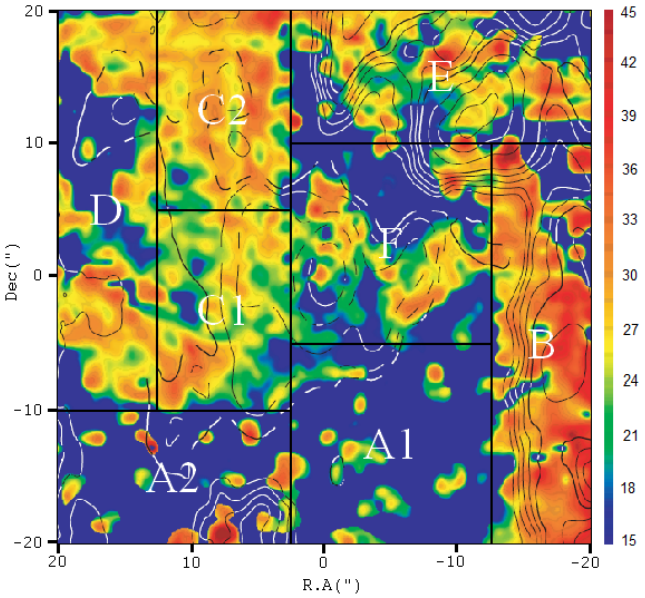


**Figure 6.** Extinction towards the ionized gas in the galactic center, as derived in Scoville et al. (2003, their Fig. 5) from the ratio of their measured Pa$\alpha$ emission to the H92$\alpha$ radio recombination-line emission of Roberts & Goss (1993). The colours show extinction in the V-band according to the scale shown; dark blue signifies no information because of insufficient H92$\alpha$ flux. The field is split into eight cells, taking into account the outline of the mini-spiral, the shape of the VHs in $v_l$ and the $\delta A_K$ curves.

the dust within the NSC. Fig. 5 shows this for the central field. We notice that the average differential extinction as a function of $v_l$ is negative for positive velocities (preferentially at the front of the cluster) and positive for negative velocities (back of the cluster) i.e., stars at the front of the cluster are observed with less extinction than their neighbors. This finding is consistent with the asymmetry of the VHs in $l$ direction (Fig. 1) and implies $A_K \simeq 0.4$ within the NSC, see below. In contrast the average differential extinction versus $v_b$ is relatively flat and consistent with the symmetric bell shape of the VH in $b$ direction. However we still notice a scatter of the points which is indicative of the systematic variations we should expect in $A_K$.

Hot dust in the central parsec has been observed with mid-infrared emission (e.g., Lau et al. 2013). The emission traces dust at the inner edge of the circumnuclear disk (CND) and in the ionized streamers collectively called the minispiral (see Fig. 3, Lau et al. 2013). Fig. 6 shows a variable extinction distribution in our central field which overlaps this region. This figure was constructed by Scoville et al. (2003) using the ratio of their Pa$\alpha$ emission measurements to the H92$\alpha$ radio recombination-line emission observed by Roberts & Goss (1993). The coloring signifies *total* extinction including foreground along the line-of-sight and the contours show the outline of the mini-spiral. Dark blue colour indicates insufficient signal-to-noise in the H92$\alpha$ emission. The outline of the mini-spiral can be seen in this extinction map, and the variability of the dust extinction along the minispiral suggests that a fraction of this extinction is likely to be associated with the mini-spiral itself and therefore is located within the NSC. The outline of the minispiral in this map and in the MIR emission is closely similar, but the ratio of emission to extinction is not constant. In some regions outside the minispiral, particularly at larger radii, dust extinction is inferred from the ratio of Pa$\alpha$ to 6cm radio continuum emission (Scoville et al. 2003), presumably arising at least partially from colder dust in the surrounding CND. These considerations will motivate our choice of subfields for which we will construct separate dust models in Section 5. For the development of the dust modeling in the next section we note that dust associated with the minispiral is likely to be concentrated in a small distance interval along the line-of-sight of order a fraction of the radius in the sky.

## 4 DUST MODELING

We saw in the previous section that the observed asymmetry of the VH in $v_l$ is likely to be associated with dust extinction. In this section we describe how one can make an analytical dust extinction model and use it with an already existing model of the NSC similar to that of section 2.

For the rest of this work, along with $l$ and $b$ we use a Cartesian coordinate system $(x, y, z)$ where $z$ is parallel to the axis of rotation as before, $y$ is along the line of sight (smaller values closer to the earth) and $x$ is along the direction of negative longitude, with the center of the NSC located at the origin.

First we need to model a luminosity function. We can do that by taking the product of two functions. The first represents a power law function in luminosity, corresponding to an exponential magnitude distribution, $L(m) = 10^{\gamma \cdot m}$. The second is an error function that represents the completeness function, so that:

$$\frac{dN}{dm} = L(m) \times C(m) = \\ 10^{\gamma \cdot m}(1 - \mathrm{erf}[(m - m_0)/\sigma])/2 \quad (2)$$

Here $\gamma$ is the power law index of the luminosity function and $m_0$ is the value where the completeness function $C(m)$ has its half height. For the power law we set the index to $\gamma = 0.27 \pm 0.02$ as in Schödel et al. (2010). For the completeness function we set $m_0 = 16.5$ and $\sigma = 1$ because we found that these values represent well the K luminosity data as shown in Figure 7. The red curve of Figure 7 shows equation 2 with the chosen values. We have also investigated models in which we approximated the red clump bump at $K_S \simeq 16$ in Fig. 7 by an additional Gaussian term. This led to $\sim 10\%$ increase in the derived $A_K$ values. Since this is below the accuracy of our determinations, we use the simpler power-law luminosity function model in the following.

Next we need the extinction variation over the line-of-sight which is just the derivative of the extinction over the line-of-sight i.e. $da_K/dy$. The function $da_K/dy$ is general and could for example be represented as a sum of Gaussians but for simplicity we choose a square function, so that:

$$\frac{da_K}{dy} = \begin{cases} 0, y < y_1 \\ c, y_1 \leqslant y \leqslant y_2 \\ 0, y > y_2 \end{cases} \quad (3)$$

in which $y_1$ and $y_2$ indicate the positions where the dust starts and ends respectively. The integral of eq.3 over all line-of-sight is the maximum extinction $A_K$ thus the constant c takes the value $c = A_K/\Delta y$ where $\Delta y = y_2 - y_1$. Function 3 integrates to:

$$a_K(y) = \begin{cases} 0\ ,\ y < y_1 \\ \frac{A_K}{\Delta y}\left(y - y_1\right), y_1 \leqslant y \leqslant y_2 \\ A_K\ ,\ y > y_2 \end{cases} \quad (4)$$

The percentage reduction in observed stars as a function of line-of-sight distance is:

$$p(y) = \frac{\int L(m - a_K(y))C(m)dm}{\int L(m)C(m)dm} \quad (5)$$

With this we can calculate the percentage reduction in numbers of stars after extinction, $p_{\max} = p(y_2)$. The percentage of stars hidden by extinction for $A_K = 0.4$ is about 25%. For the simple case where the luminosity function is a power law, the previous equation (5) takes the form $p(y) = L(-a_K(y))$. The function for $A_K = 0.4$ is shown in figure 8.

Having that we calculate the $\mathrm{VP}_l$ including the effect of dust extinction, denoted by VPD:

$$\mathrm{VPD}(\upsilon_l; x, z) = \frac{1}{\Sigma} \iiint_{E>0} p(y) f_{tot}(E, L_z)\, d\upsilon_{los} d\upsilon_z dy. \quad (6)$$

Here $\Sigma$ is the stellar surface density of the NSC model, and $f_{tot}(E, L_z) = f_e(E, L_z) + f_o(E, L_z)$ is the total DF, consisting of an even part in $L_z$ (contributing to the density) and an odd part (contributing to rotation), as in Chatzopoulos et al. (2015). Figure 9 shows typical VPDs after adding dust with $A_K = 0.4$. We observe that the right peak of the $\mathrm{VP}_l$ is now higher than the left peak which is a combined effect of dust and rotation. The dust does not produce an asymmetry for the VP in the $b$ direction. One useful quantity is $A_K(\upsilon_l)$ averaged over the line-of-sight. This can be calculated with

$$\langle A_K(\upsilon_l; x, z)\rangle = \frac{\iiint a_K(y) p(y) f_{tot}\left(E, L_z\right) d\upsilon_z d\upsilon_{los} dy}{\Sigma \times \mathrm{VPD}\left(\upsilon_l\right)} \quad (7)$$

for each line-of-sight and connects our model with the photometry. From this we calculate the average differential extinction between stars of given $\upsilon_l$ and their neighbors, which corresponds to the data of Fig. 5:

$$\delta A_K(\upsilon_l; x, z) = \langle A_K(\upsilon_l)\rangle - \frac{\int \langle A_K\left(\upsilon_l\right)\rangle \mathrm{VPD}\left(\upsilon_l\right) d\upsilon_l}{\Sigma \int \mathrm{VPD}\left(\upsilon_l\right) d\upsilon_l} \quad (8)$$

In order to understand the effects of dust extinction on $\delta A_K(\upsilon_l)$, we use two simple models for the dust distribution. The first is a homogeneous dust model that extends a few parsecs along the line-of-sight. The second is a thin $\sim 10''$ screen of dust placed at several positions along the line-of-sight. We have verified that the width of the screen is not a sensitive parameter and the results are almost unchanged if we set it for example to $\sim 5''$. Figures 9 and 10 shows these effects. In Fig. 9 we see the effect of three dust screen models and one homogeneous model on the $\mathrm{VP}_l$ for $A_K = 0.4$.

One important point to notice is that we can achieve the same effect (e.g. the same amount of asymmetry in the histograms) with several models by using different combinations of $A_K$ and the distances at which the dust is placed along the line-of-sight , therefore the dust extinction model is degenerate. In Fig. 10 we see plots of several screen and homogeneous models based on eq. 8. The top panels show the $\delta A_K(\upsilon_l)$ curves of a screen dust model placed at several distances in front of (left) and at the back (right) of the cluster for $A_K = 0.4$. The first thing to notice is that the further the screen of dust is placed from the center the smaller is the effect of dust. This makes sense since far from the center the density of stars is lower. We also note that if the screen of dust is placed in front of the cluster, the curves are close to constant for the stars behind the cluster (i.e., for negative $\upsilon_l$) since there is no dust there to affect the $\delta A_K(\upsilon_l)$. The opposite happens when the screen of dust is behind the cluster. The bottom left panel shows the shape of $\delta A_K(\upsilon_l)$ for different $A_K$. The bottom right panel shows three homogeneous models that extend over different distance intervals along the line-of-sight. In this case the curves are symmetric relative to zero. The dust extinction model was implemented with Wolfram Mathematica ().

## 5 PREDICTIONS OF THE DUST MODEL

In the last section we described how one can include the effects of dust extinction in the dynamical modeling of the NSC, and calculated differential reddening signatures for the NSC stars. Here we proceed to model predictions and compare with both photometric and kinematic evidence. We will see that the asymmetries seen in the VPs for $\upsilon_l$ can be explained as due to dust within the NSC. Our goal is to see whether dust in the Galactic Center mini-spiral can explain our data, and also to provide a rough extinction map of the central field based on the model and the available data.

As discussed in Section 3.2, MIR observations (see the MIR map of Lau et al. 2013) show that hot dust is associated with the minispiral within the NSC although it cannot be assumed to trace the dust extinction directly. Figure 6 based on Figure 5 of Scoville et al. (2003) shows the total dust extinction in the central $40'' \times 40''$ around Sgr A*, derived from the observed ratio of Pa$\alpha$ to H92$\alpha$ radio recombination-line emission. This map includes both foreground and NSC extinction. It shows the outline of the minispiral because it is

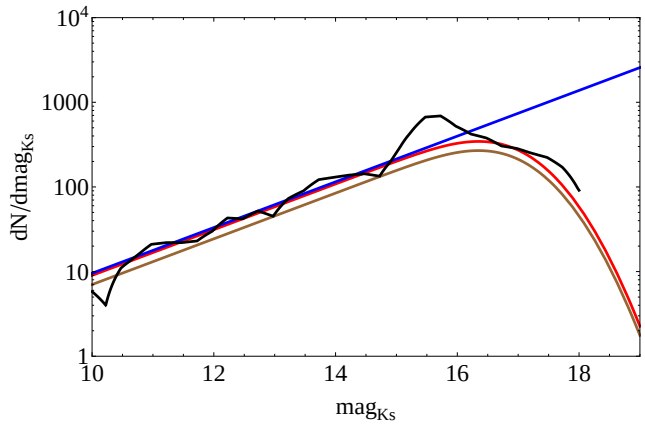


**Figure 7.** Modeled K-band luminosity function without and with dust extinction. The blue line shows a power law fit to the stars $11 < K < 14$ with power-law index of $0.27 \pm 0.02$ as in Schödel et al. (2010). The red line shows the effect of the completeness function. The brown curve is the red curve shifted faintwards by $A_K = 0.4$ dust extinction. The black line shows the K luminosity function for the Galactic center stars.

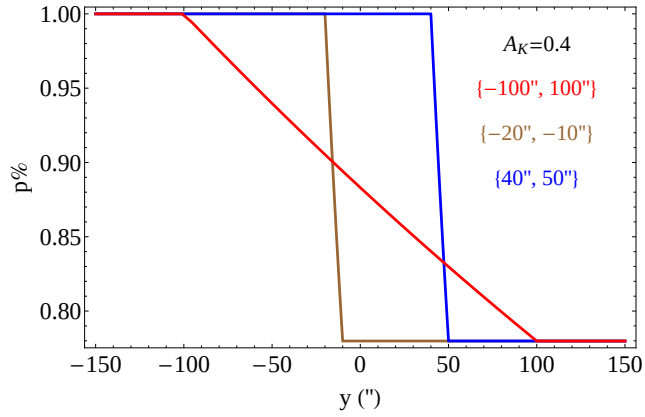


**Figure 8.** Percentage reduction in observable stars after a dust effect with $A_K = 0.4$. as a function of line-of-sight for a homogeneous dust model (red) and two dust screen models (brown, blue). About 75% of stars remain in the observed luminosity function after the extinction due to dust.

limited by the signal-to-noise ratio (S/N) of the H92$\alpha$ recombination line flux, and the regions in which the extinction has an apparent value of $A_V = 15$ is where the S/N is not sufficient to derive the extinction. Fig. 6 shows the greatest extinction in front of the Western arm, and relatively low extinction in front of the east-west bar. This suggests, in addition to possible foreground extinction, position-dependent extinction associated with the minispiral itself.

For our modelling, Fig. 6 is split into eight cells and subcells. The reasoning behind the choice of these cells is based on the outline of the mini-spiral, but also on the statistics and shape of the velocity histograms in $\upsilon_l$ and the mean differential extinction variation $\delta A_K$ along line-of-sight in these cells. Some cells cover the region outside the minispiral

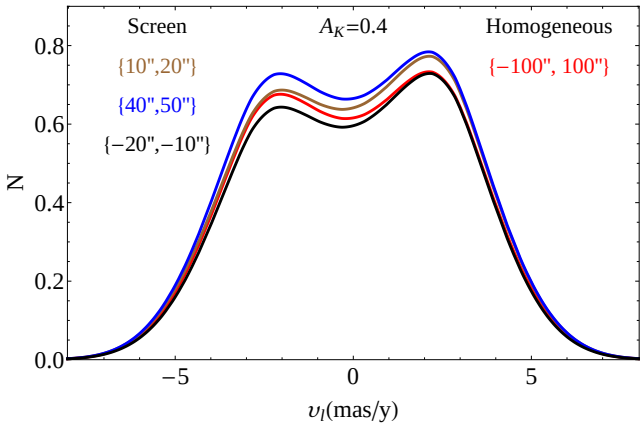


**Figure 9.** VPDs in $l$ direction for different dust distribution models, as indicated on the plot. The right peak is higher due to the combined effects of dust extinction and rotation. We can achieve the same effect (e.g. the same asymmetry) for several combinations of $A_K$s and the distances where the dust is placed along the line-of-sight. All VPDs are for a line-of-sight with $l = 10''$ and $b = 10''$.

where the observed ratio of Pa$\alpha$ to 6 cm radio continuum emission (Scoville et al. 2003) also shows extinction, possibly in the foreground. This will also be tested by our modelling. The VH$_l$s for all cells and the $\delta A_K$ as a function of $\upsilon_l$ and $\upsilon_b$ are shown in Fig. 11 for the following cells:

- Cell A1: This cell's small $\delta A_K$ values are consistent with the lack of features in the extinction map in comparison with other cells. Also the $\delta A_K$ values are consistent with the VH$_l$ since both peaks look symmetric which is a sign of lack (or small amount) of dust within the NSC.
- Cell A2: The cell lacks strong mini-spiral features as cell A1. However both the VH$_l$ and $\delta A_K$ values show stronger effects of dust therefore this cell is separated from cell A1.
- Cell B: The $\delta A_K$ values and the VH$_l$ are consistent with the strong features of the mini-spiral in the extinction map since the $\delta A_K$ points are higher and lower for negative and positive velocities respectively than the other cells and the asymmetry of the VH$_l$ is intense. We also note that the dust effects are similar within the whole area B because after splitting it into 2 sub-areas (not shown) we observed the same signature.
- Cells C1 & C2: The cells C1 and C2 belong to the Northern Arm of the mini-spiral. The shape of the $\delta A_K$ data for both cells seems similar for negative velocities but the $\delta A_K$ for C2 is more symmetric and consistent with the extinction map hence we split the area into 2 halves. We notice also some asymmetry on the VH$_l$s of both areas C1 and C2.
- Cell D was separated from C1 & C2 because the $\delta A_K$ values look more symmetric than C1 & C2. We also note that the dust effects are similar within the whole area D because after splitting it into 2 sub-areas (not shown) we observed the same signature.
- Cells E & F: The $\delta A_K$ values of these two cells look similar but the VH$_l$ of the cell F lacks the asymmetry char-

acteristic in contrast of cell E therefore we keep them separate.

The central field with these eight cells is surrounded by a a more extended area with observations for about 2000 stars. We split this area into three outer fields O1-O3 placed around the central field as shown in Fig. 3. The $\mathrm{VH}_l$ for these cells and the $\delta A_K$ as a function of $\upsilon_l$ are shown in Fig. 12.

Our goal is to give a model prediction of each of these cells (8+3 in total). For the model we use a thin screen of dust with width $10''$ because the dust associated with the minispiral is likely to be concentrated in a small distance interval along the line-of-sight. The precise width of the dust screen is not important as the dust signatures are insensitive to this parameter. The two main parameters are the total extinction in the screen and its location along the line-of-sight. However, as explained in the last section, these two parameters are partially degenerate. The degeneracy is particularly strong for the $\mathrm{VH}_l$ histograms. The $\delta A_K$ data in principle are sensitive to whether the extinction is in front or behind the Galactic center, as shown in Fig. 10. However, the $A_K$ data have large scatter between adjacent data points such that points with seemingly small error bars can even have the 'wrong' sign of $\delta A_K$ (Fig. 11). This large scatter is also seen in the $\delta A_K$ versus $\upsilon_b$ plots (also shown in Fig. 11) where no dust signature is present. Therefore we decided to not try to fit the data using $\chi^2$.

Rather, we choose to place the dust screens along the line-of-sight according to other available information, and only deviate from this when this appears inconsistent with the shape of the $\delta A_K$ distribution. The total dust extinction of the dust screen is then chosen by eye mostly from the amplitude and shape of the $\delta A_K$ distribution, taking into account also the scatter of the $\delta A_K$ points, and to a lesser degree from the asymmetry of the $\mathrm{VH}_l$ peaks.

Specifically for the central field we use the three orbit-model of Zhao et al. (2009) for the three ionized gas structures in the central 3pc (the Northern Arm, Eastern Arm, and Western Arc). We then map the center of each of the cells to a point in the relevant orbit plane according to its R.A and Dec. position. The distance from the center along the line-of-sight is given from the coordinates of that point on the orbit plane. For each cell, we use one common mean distance. Table 1 shows to which orbital plane each cell is assigned, and the distance of the dust screen from Sgr A*.

Fig. 11 shows the predictions of the screen dust model for the 8 cells of the central field. The reasoning behind the choice of $A_K$ and positions for the dust screen is based on the shape of the data and the examples of Fig. 10:

- Cell A1 & B: We place the dust screen in front of the cluster according to the value of Table 1. These two cells are interesting because they both show a correlation between the outline of the mini-spiral and the photometry data. They also exhibit the maximum contrast between the amount of dust. Cell B needs $\sim 5$ times more extinction than cell A.
- Cell A2: The dust screen is placed behind the center according to Table 1.
- Cell C1 & D: The shape of the data in conjunction with the top right panel of Fig. 10 indicate that the dust screen should be behind the cluster (also gives a much better $\chi^2$) in contrast with the value of Table 1. A possible reason for this could be that the single orbit description is not accurate for the centers of these cells.
- Cell C2 & E: For both cells the dust screen is placed in front of the cluster according to Table 1.
- Cell F: The shape of the data in conjunction with the lower right panel of Fig. 10 indicate that the dust screen should be centered.

| | | | | |
|---|---|---|---|---|
| Northern Arm | E (-15") | | | |
| Eastern Arm | A2 (5") | C1 (-9") | C2 (-25") | D (-20") |
| Western Arc | B (-25") | A1 (-10") | F (-5") | |

**Table 1.** Each one of the eight cells of Fig. 10 belongs to an orbital plane (Zhao et al. 2009) representing one of the three ionized gas (Northern Arm, Eastern Arm, and Western Arc) formations. The inferred line-of-sight distance of the dust screen from Sgr A* is given in the parentheses (negative points towards the earth).

For the outer cells of the extended field the $A_K$ is selected according to the general characteristics of plot 10:

- Cell O1: the VHs and the photometry have a consistent signature. The extinction is close to $A_K \simeq 0.4$ mag.
- Cells O2 and O3: For these cells the photometry gives $A_K \simeq 0.3$ and 0.35 but the peaks of the VHs are almost symmetric.

Based on the model of the CND in Lau et al. (2013), we might have expected stronger extinction effects in fields O1 and O3 than in O2. However, this is not confirmed by Fig. 10 and the lack of correspondence between the $\delta A_K$ and the VHs is puzzling.

Having the prediction for the cells we can estimate the foreground extinction for each cell using the $A_K$ values of Fig. 3. The second row of table 2 shows the total extinction of each cell of the central field based on Fig. 3. The third row shows an estimate of the foreground extinction based on $A_K(\mathrm{total}) = A_K(\mathrm{foreground}) + x * A_K(\mathrm{NSC})$ where we approximate $x = 0.5$ to take into account that of order half of the stars are unobscured because they are in front of the cluster. The exact value is not important for the scope of this paper but it should be closer to $x = 0.5$ than $x = 1$.

## 6 DOES THE ADDITION OF DUST AFFECT THE MEASURED $M_\bullet$, $M_*$ AND $R_0$?

In this section we try to answer how much the dust *within* the NSC will affect the derived (Chatzopoulos et al. 2015) statistical parallax, supermassive black hole and stellar mass of the NSC. The *foreground* dust will affect the VPs only by a scale factor which does not impact the derived values. In Chatzopoulos et al. (2015) we derived new constraints on the $R_0$, $M_*$ and $M_\bullet$ by fitting to the corresponding data the $\left\langle \upsilon^2 \right\rangle^{1/2}_{l,b,los}$ parts of the $2^{nd}$ order Jeans moments, that are moments of the even part of the corresponding VPs of the 2-Integral distribution function. Therefore here the problem is reduced to how much the even part in $L_z$ of the VPs changes after the addition of dust within the NSC.

Figure 13 shows the even parts of the VPs for $\upsilon_l, \upsilon_b$ and $\upsilon_{los}$ for the NSC dynamical model from Chatzopoulos et al. (2015) with best mass and distance parameters,

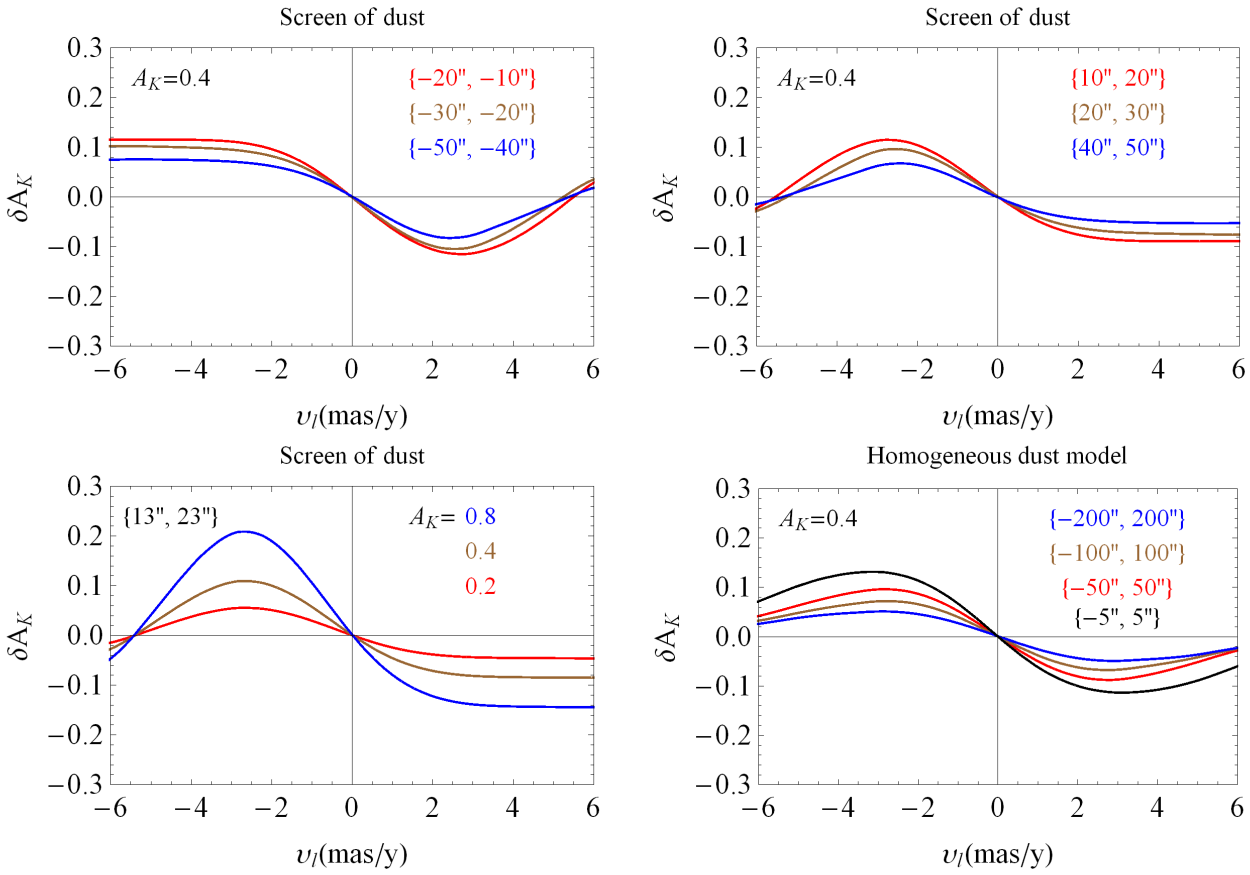


**Figure 10.** Shape of $\delta A_K$ versus $\upsilon_l$ curve for several dust models. Top left: in front of the cluster for constant $A_K = 0.4$. The numbers in the parenthesis show where the dust screen starts and ends respectively along the line-of-sight. Top right: Dust screen models placed behind the cluster for constant $A_K = 0.4$. Bottom left: Dust screen models placed slightly behind the cluster for several $A_K$ values. Bottom right: Homogeneous dust models that extend over different distances ranges along the line-of-sight for constant $A_K$. The line-of-sight for all curves has coordinates $l = 10''$ and $b = 10''$.

| Cell | A1 | A2 | B | C1 | C2 | D | E | F |
|---|---|---|---|---|---|---|---|---|
| Total extinction | 2.73 | 2.99 | 3.1 | 2.82 | 2.87 | 2.78 | 2.84 | 2.95 |
| Foreground extinction | 2.66 | 2.79 | 2.7 | 2.67 | 2.72 | 2.61 | 2.69 | 2.8 |

**Table 2.** Extinction values per cell based on Fig. 3. The foreground extinction of each cell is estimated according to $A_K(\text{total}) = A_K(\text{foreground}) + x * A_K(\text{NSC})$ where we approximate $x = 0.5$ to take into account that of order half of the stars are unobscured because in front of the cluster. The exact value is not important for the scope of this paper but it should be closer to $x = 0.5$ than $x = 1$.

and for the same dynamical model including the screen dust prediction, for a line-of-sight through cell B which has the largest amount of extinction ($A_K = 0.8$) among the cells of the central and outer fields. We notice that the difference between the VPs for this amount of extinction is very small. Specifically the average difference of the $2^{nd}$ moments of the VPs between the two models is $\sim 1.5\%$. If instead we use $A_K = 0.4$, close to the average extinction within the NSC inferred from this work, the difference is smaller than 0.5%. The relative differences of $\sigma_{los}/\sigma_b$ and $\sigma_{los}/\sigma_l$ between the model with no dust and the model with $A_K = 0.4$ are similarly small, 0.2% and 0.6%, respectively. Therefore we conclude that the systematic effects on the statistical parallax due to dust are within the estimated errors of Chatzopoulos et al. (2015), causing the distance to the NSC to decrease by $\sim 0.4\% \simeq 30$pc.

That the changes in the even part are so small can be explained by the following formal argument for the $\text{VP}_l$. We show that for small amounts ($1^{st}$ assumption) of homogenized ($2^{nd}$ assumption) dust around the center the even part of the renormalized VP in $\upsilon_l$ is the same as that for no dust. The odd part is a direct indicator of dust at

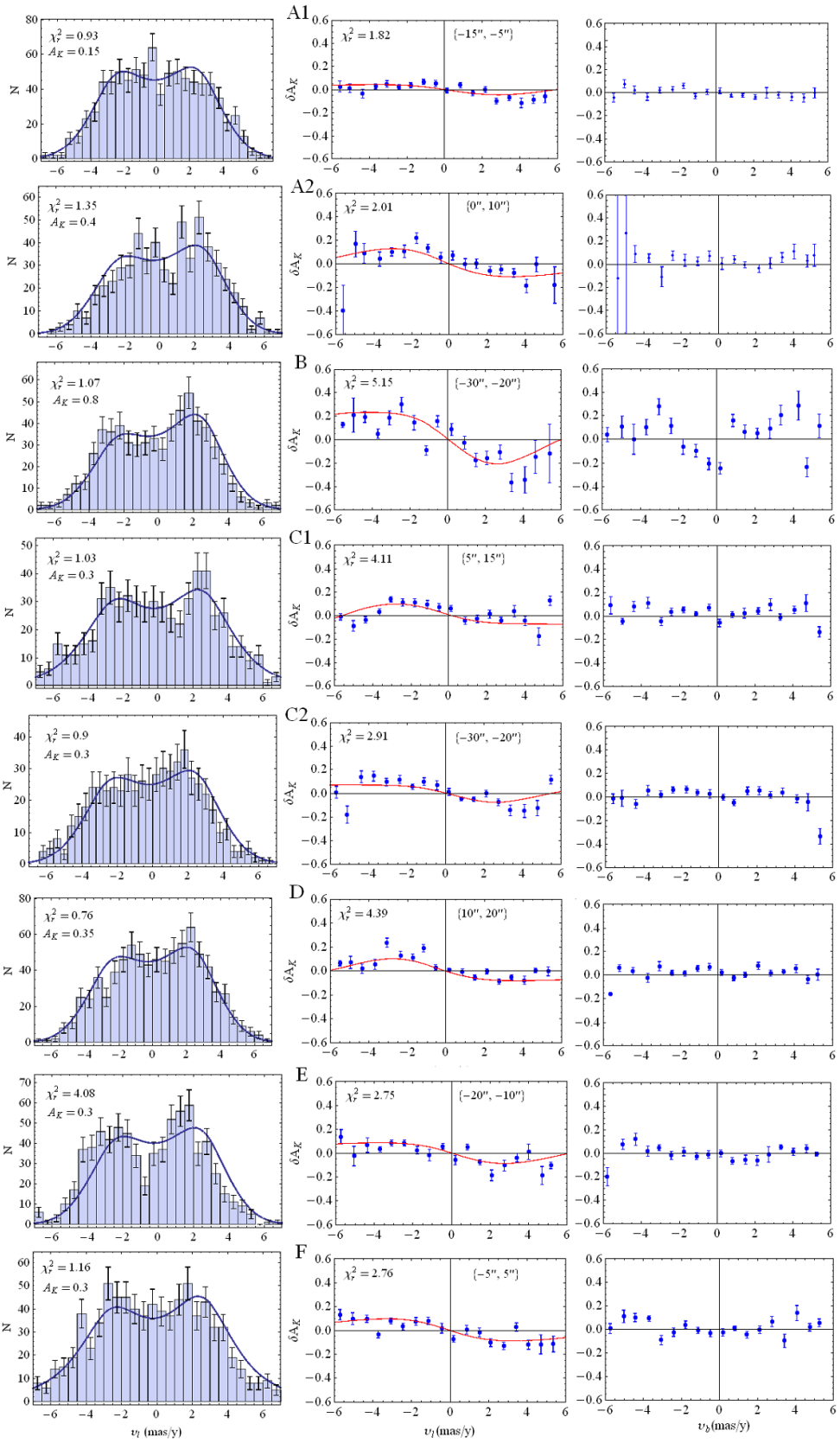


**Figure 11.** Predictions of the model with the VH and $\delta A_K$ data for each cell. The numbers in the brackets show where the screen of dust is placed relative to the center. The line-of-sight is placed at the center of each cell. Reduced $\chi^2$ are also provided for the histograms and the photometry. For the cells A1, A2, B, C2, E, the screen dust distance is based on the orbit models of the mini-spiral (Zhao et al. 2009).

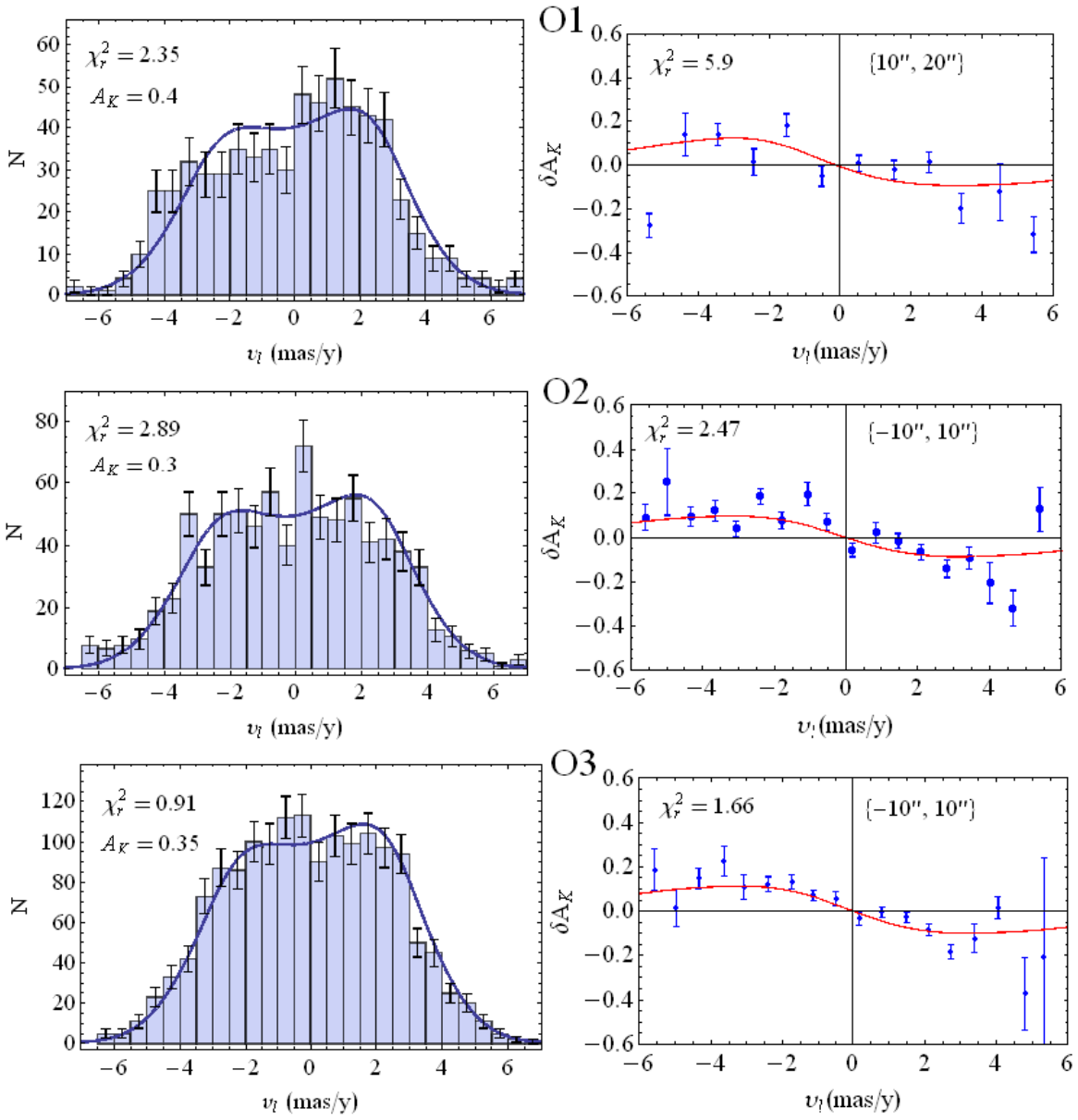


**Figure 12.** Predictions of the model with the VH and $\delta A_K$ data for the outer cells shown in Fig.3. The numbers in the brackets show where the screen of dust is placed relative to the center. The line-of-sight is placed at the center of each cell. Reduced $\chi^2$ are also provided.

that point $(l, b)$ and can be used to estimate $A_K$.

When the luminosity function is a power law and the dust is homogeneously placed i.e. $y_1 = -y_2$ in equations 3 and 4, $p(y)$ takes the form within the dust area:

$$p(y) = L(-a_K(y)) = 10^{-\gamma\left(\frac{A_K}{2} + \frac{A_K y}{\Delta y}\right)} \tag{9}$$

For small $A_K \ll (\gamma \ln(10))^{-1} \simeq 1.61$ we have:

$$\begin{aligned} p(y) &\simeq 1 - \gamma \ln(10) \tfrac{A_K}{2} - \gamma \ln(10) \tfrac{A_K}{\Delta y} y \\ &= p(0) - ky \end{aligned} \tag{10}$$

where $p(0) = 1 - \gamma \ln(10) \frac{A_K}{2}$ and $k = \gamma \ln(10) \frac{A_K}{\Delta y}$.

Therefore[1] the function $g(y) = p(y) - p(0)$ is odd everywhere (including the area where there is no dust). Next for simplicity we use $f_{tot}(E, L_z) = f(E, x v_{los} - y v_l) \to f(v_l y)$ because $y$ appears within $f$ only with the form of $y^2$ and $v_l y$.

[1] we showed this for the case where the luminosity function is a power law but the same holds in the general case $L(m)$ where $\gamma \cdot \ln(10)$ is replaced by $\frac{\int L'(m) C(m) dm}{\int L(m) C(m) dm}$.

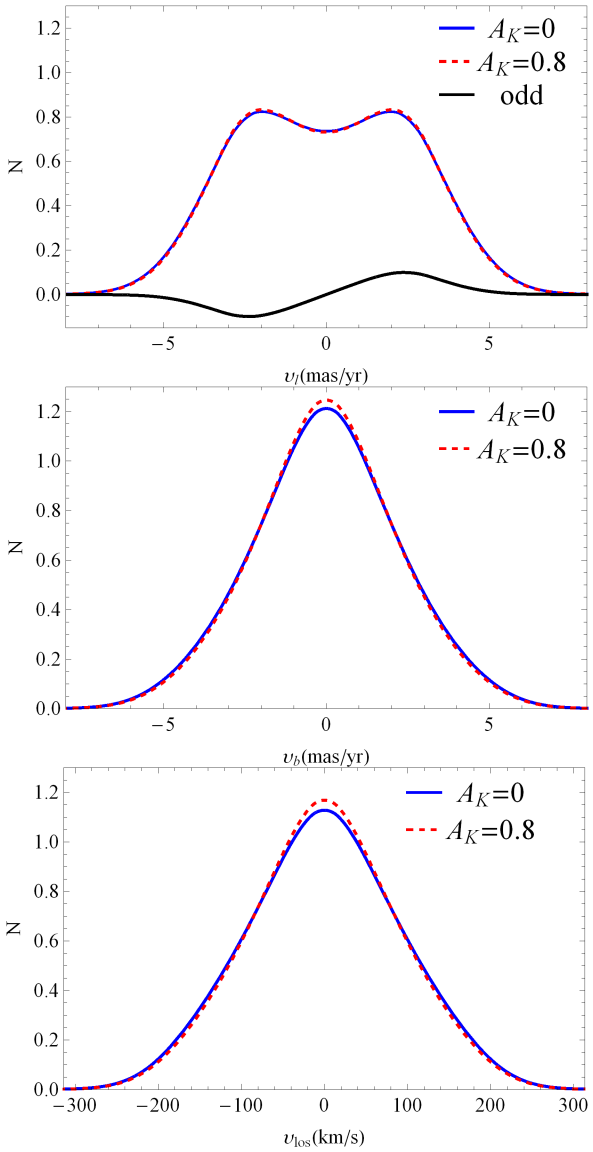


**Figure 13.** Even part of the renormalized VPs for $v_l, v_b$ and $v_{los}$ for the NSC dynamical model with no dust from Chatzopoulos et al. (2015), and for the same dynamical model including the dust screen prediction based on cell B. The black line in the upper panel corresponds to the odd part of the $\mathrm{VP}_l$. The VPs are calculated at the center of cell B.

Now we have:

$$\frac{1}{2}\int p(y)\iint \left(f(v_l y)+f(-v_l y)\right)dv_z dv_{los}dy$$
$$-\frac{1}{2}\int p(0)\iint \left(f(v_l y)+f(-v_l y)\right)dv_z dv_{los}dy = \quad (11)$$
$$\frac{1}{2}\int g(y)\iint \left(f(v_l y)+f(-v_l y)\right)dv_z dv_{los}dy = 0$$

The previous is 0 because $g(y)$ is an odd function and $\iint \left(f(v_l y)+f(-v_l y)\right)dv_z dv_{los}$ is an even function of $y$ therefore:

$$\frac{1}{2}\int p(y)\iint \left(f(v_l y)+f(-v_l y)\right)dv_z dv_{los}dy = \quad (12)$$
$$\frac{1}{2}p(0)\iiint \left(f(v_l y)+f(-v_l y)\right)dv_z dv_{los}dy$$

And thus:

$$\mathrm{VPD}_{\mathrm{even}}(v_l) = p(0)\mathrm{VP}_{\mathrm{l}}(v_l) \quad (13)$$

To find the constant $p(0)$ we integrate once more over the velocity this time:

$$\int \mathrm{VPD}_{\mathrm{even}}(v_l)dv_l = p(0)\int \mathrm{VP}_{\mathrm{l}}(v_l)dv_l = p(0) \quad (14)$$

Therefore $p(0)$ is the normalization factor of the $\mathrm{VPD}_{\mathrm{l}}$. The above means that to first order, dust does not affect the even part of the VPD in $l$ direction significantly except for a scale factor. Fig 13 shows that the effects for $\mathrm{VPD}_{\mathrm{b}}$ and $\mathrm{VPD}_{\mathrm{los}}$ are similarly small. If extinction within a stellar system is small enough ($A_K \ll 1.6$ for the NSC) then fitting the even part of a model's VPs to the even part of the VHs is sufficient to get accurate estimates of the $M_\bullet$, $M_*$ and $R_0$ parameters. In Chatzopoulos et al. (2015) we used the root mean square velocities that are moments of the even parts of the VHs to fit the $M_\bullet$, $M_*$ and $R_0$ parameters of the axisymmetric model. Therefore we expect that their values will not be affected by dust more than 0.4% as we explained earlier.

In principle the odd part of the $\mathrm{VPD}_{\mathrm{l}}$ can be fitted to the odd part of the VHs and this part is scale free since the scaling factor is already known from the even part therefore one can fit the $A_K$ for some combination of cells.

## 7 DISCUSSION & CONCLUSIONS

The main goal of this work was to understand the slight asymmetries in the $\mathrm{VP}_l$s of the NSC and their influence on the dynamical modeling following the recent work of Chatzopoulos et al. (2015). Our interest was triggered by the observation that the right peak of the $\mathrm{VH}_l$ is often slightly higher than the left. A plausible explanation was given based on the existence of dust *within* the NSC. Because of the dust, the apparent number of stars behind the NSC is smaller than that in front of the cluster. This in conjunction with the rotation can explain the observed characteristic.

In order to quantify the dust effects, we worked with proper motions and photometry for $\sim 7100$ stars from Fritz et al. (2014). We applied an analytic dust extinction model together with our recent NSC dynamical model. The extinction model gave us reasonable results and was able to predict both the signature in the VPs and the photometry.

Observation of the NSC in the optical is almost impossible because of 30 mag extinction. In the infrared the situation is much better since $A_K \sim 3$ mag. Most of this extinction belongs to the foreground and does not affect the shape of the VHs (except a normalization factor). We find here that a small fraction of the total extinction value ($\sim 15\%$) belongs within the NSC.

The area between $\sim 1-1.5$pc radius consists of several streamers of dust, ionized and atomic gas with temperatures between $100K - 10^4K$ and is called "ionized central cavity" (Ekers et al. 1983). The mini-spiral is a feature of the ionized cavity, and is formed from several streamers of gas and dust infalling from the inner part of the CND (Kunneriath et al. 2012). It consists of four main components: the Northern arm, the Eastern arm, the Western arm and the Bar (Zhao et al. 2009) that can be described well by streams of ionized gas or filaments orbiting Sgr A* (Serabyn & Lacy 1985).

We investigated how well the mini-spiral correlates with the extinction effects in the NSC data within the central field. To assess this we first investigated whether our extinction model puts the dust on the same side of the NSC as does the mini-spiral interpretation. This is true for six out of the eight cells (except cell C2). We found the largest extinction ($A_K = 0.8$) in cell B where also the largest extinction is inferred from the extinction map of Scoville et al. (2003), and particularly low extinction in cell A where the extinction map is consistent with only foreground extinction.

We can estimate the mass that corresponds to a given amount of extinction using

$$\rho_d = \frac{A_K}{\Delta y} \frac{1}{1.086 \kappa_\lambda} \tag{15}$$

where $\rho_d$ is the dust density, $\kappa_\lambda = 1670 \mathrm{cm}^2/\mathrm{g}$ (Draine 2003a) is the mass extinction coefficient [2] for the K-Band, $A_K = 0.4$ from the model prediction and $\Delta y = 10''$ is the width of the dust screen. We find that $\rho_d \simeq 1.8 \times 10^{-19} \mathrm{kg/m}^3$ and the dust mass within a parallelepiped with dimensions $(10'', 40'', 40'')$ centered on Sgr A* is $M_d \sim 3 M_\odot$. Since the dust extinction model presented here is not precise we consider that this estimate is correct only within an order of magnitude. This value is within the range of $0.25 - 4 M_\odot$ for the mini-spiral found from other works (Zylka et al. 1995; Kunneriath et al. 2012; Etxaluze 2011).

Finally we showed that for small values of extinction the even parts of the VPs are not affected significantly. As a result, the measured $M_\bullet$ and $M_*$ parameters of Chatzopoulos et al. (2015) do not change by more than $\sim 0.4\%$ for extinction $A_K \simeq 0.4$ and the inferred $R_0$ is decreased by the same amount, which is less than the smallest systematic error (for the statistical parallax) inferred for these parameters in Chatzopoulos et al. (2015).

Our results can be summarized as follows:

- We showed that extinction due to dust explains kinematic asymmetries and differential photometry of the NSC, and measured the amount of extinction within the NSC by combining a dynamical model with a dust extinction model.
- We presented an extinction table for the dust *within* the NSC in several cells.
- We found that the distribution of the dust is consistent with the extinction being associated with the mini-spiral for six out of eight cells.
- Systematic effects due to dust with typical extinction $A_K \simeq 0.4$ affect the $M_\bullet$, $M_*$ and $R_0$ parameters deduced from previous dynamical modeling only by $\simeq 0.4\%$, which is smaller than their estimated systematic errors.

## REFERENCES


Antonini F., 2013, ApJ, 763, 62
Antonini F., Capuzzo-Dolcetta R., Mastrobuono-Battisti A., Merritt D., 2012, ApJ, 750, 111
Arca-Sedda M., Capuzzo-Dolcetta R., 2014c, MNRAS, 444, 3738


[2] ftp://ftp.astro.princeton.edu/draine/dust/mix/kext_albedo_WD_MW_3.1_60_D03.all


Bahcall J. N., Wolf R. A., 1976, ApJ, 209, 214
Bartko H., et al. 2010, ApJ, 708, 834
Böker T., Laine S., van der Marel R. P., et al., 2002, AJ, 123, 1389
Böker T., Sarzi M., McLaughlin D. E., et al., 2004, AJ, 127, 105
Buchholz, R. M., Schodel, R., Eckart, A. 2009, A&A, 499, 483
Carollo, C. M., Stiavelli, M., & Mack, J. 1998, AJ, 116, 68
Chatzopoulos S., Fritz T. K., Gerhard O., Gillessen S., C. Wegg, Genzel R., Pfuhl O., 2015 MNRAS 447, 948C
Christopher, M. H., Scoville, N. Z., Stolovy, S. R., & Yun, M. S. 2005, ApJ, 622, 346
Dehnen W., 1993 MNRAS 269, 250
Draine, B.T. 2003a, ARA&A, 41, 241
Ekers, R. D., van Gorkom, J. H., Schwarz, U. J., & Goss, W. M. 1983, A&A, 122, 143
Etxaluze, M., Smith, H. A., Tolls, V., et al. 2011, AJ, 142, 134
Ferrarese L., Côtè P., Jordan A., et al., 2006, ApJS, 164,334
Fritz T. K., et al. 2011, ApJ, 737, 73
Fritz T. K., Chatzpoulos S., Gerhard O., Gillessen S., Dodd-Eden K., Genzel R., Ott T. Pfuhl O., Eisenhauer F., 2014, arXiv:1406.7568v1, submitted
Genzel R., Eisenhauer S., Gillessen S. 2010, Reviews of Modern Physics 82, 3121
Ghez A., et al., 2008, ApJ, 689, 104
Gillessen S., Eisenhauer S., Trippe S, Alexander T., Genzel R., Martins F., Ott T, 2009, ApJ, 707, L11
Jackson J. M., Geis N., Genzel R., Harris A. I., Madden S., Poglitsch A., Stacey G. J., Townes C. H., 1993, ApJ, 402, 173
Kunneriath, D., Eckart, A., Vogel, S. N., Teuben, P., Muzi, K. A&A, 538, A127
Lau R.M., Herter T.L., Morris M.R., Becklin E.E., Adams J.D. ApJ, 775, 37
Pfuhl, O., Alexander, T., Gillessen, S., et al. 2014, ApJ, 782, 101
Preto M. & Amaro-Seoane P. 2010 ApJ 708, L42-L46.
Rieke, G. H., & Rieke, M. J. 1988, ApJL, 330, L33
Roberts, D. A. & Goss, W. M. 1993, ApJ, 86, 133
Rossa J., van der Marel R. P., Böker T., et al., 2006, AJ, 132, 1074
Schödel R., Merritt D., Eckart A.,2009, A&A, 502, 91
Schödel R., Najarro F., Muzic K., Eckart A., 2010, A&A, 511, A18
Schödel R., Feldmeier A., Kunneriath D., Stolovy S., Neumayer N., Amaro-Seoane P., Nishiyama S., 2014, A&A, 566, 47S
Scoville, N. Z., Stolovy, S. R., Rieke, M., Christopher, M., & Yusef-Zadeh, F. 2003, ApJ, 594, 294
Serabyn, E., & Lacy, J. H. 1985, ApJ, 293, 445
Seth A. C., Dalcanton J. J., Hodge P. W., Debattista V. P., 2006, AJ, 132, 2539
Seth A., Agueros M., Lee D., Basu-Zych A., 2008, ApJ, 678, 116
Schinnerer E., Boker T., Meier D. S., Calzetti D., 2008, ApJ, 684, L21
Tremaine S. D., Ostriker J. P., Spitzer L., Jr, 1975, ApJ, 196, 407
Tremaine S., Richstone, D. O., Byun, Y., Dressler, A., Faber, S. M., Grillmair, C., Kormendy, J., Lauer, T. R.

1994, AJ, 107, 634
Qian E.E, de Zeeuw P.T., van der Marel R.P., Hunter C. 1995, MNRAS 274, 602
Walcher C. J. et al., 2005, ApJ, 618, 237
Wehner E. H., Harris W. E., 2006, ApJL, 644, L17
Zhao, J.-H., Morris, M. R., Goss, W. M., & An, T. 2009, ApJ, 699, 186
Zylka R.,Mezger P. G.,Ward-Thompson D.,DuschlW. J., Lesch H., 1995, A&A, 297, 83
Wolfram Research, Inc., Mathematica, Version 8.0, Champaign, IL (2011)